ACS APPLIED MATERIALS & INTERFACES

Research Article

www.acsami.org

Simple Synthesis of Amorphous $NiWO_4$ Nanostructure and Its Application as a Novel Cathode Material for Asymmetric Supercapacitors

Lengyuan Niu,[†,‡] Zhangpeng Li,[†] Ye Xu,[†,‡] Jinfeng Sun,[†,‡] Wei Hong,[†,‡] Xiaohong Liu,[†] Jinqing Wang,*[,†] and Shengrong Yang[†]

[†]State Key Laboratory of Solid Lubrication, Lanzhou Institute of Chemical Physics, Chinese Academy of Sciences, Lanzhou 730000, PR China

[‡]University of Chinese Academy of Sciences, Beijing 100080, PR China

Supporting Information

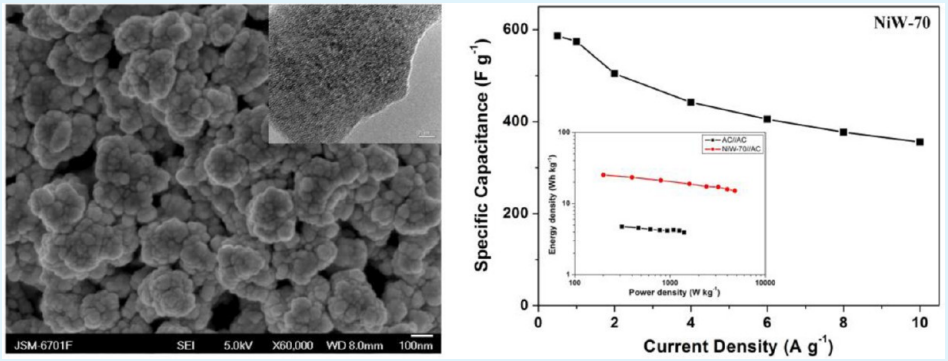

ABSTRACT: This study reports a simple synthesis of amorphous nickel tungstate ($NiWO_4$) nanostructure and its application as a novel cathode material for supercapacitors. The effect of reaction temperature on the electrochemical properties of the $NiWO_4$ electrode was studied, and results demonstrate that the material synthesized at 70 °C (NiW-70) has shown the highest specific capacitance of 586.2 F g^{-1} at 0.5 A g^{-1} in a three-electrode system. To achieve a high energy density, a NiW-70//activated carbon asymmetric supercapacitor is successfully assembled by use of NiW-70 and activated carbon as the cathode and anode, respectively, and then, its electrochemical performance is characterized by cyclic voltammetry and galvanostatic charge−discharge measurements. The results show that the assembled asymmetric supercapacitor can be cycled reversibly between 0 and 1.6 V with a high specific capacitance of 71.1 F g^{-1} at 0.25 A g^{-1}, which can deliver a maximum energy density of 25.3 Wh kg^{-1} at a power density of 200 W kg^{-1}. Furthermore, this asymmetric supercapacitor also presented an excellent, long cycle life along with 91.4% specific capacitance being retained after 5000 consecutive times of cycling.

KEYWORDS: *asymmetric supercapacitor, nickel tungstate, energy storage, electrode materials*

1. INTRODUCTION

Electrochemical energy storage devices, such as fuel cells, batteries, and supercapacitors, are an essential part of the clean energy era necessary to tackle the ever worsening fossil energy depletion and global warming issues.[1] Among the presently existing energy storage devices, supercapacitors are one of the most promising candidates because of their higher power density and fast charge−discharge rate, as well as excellent cycle stability.[2−4] However, to meet the increasing energy demands for next-generation energy storage devices, a major disadvantage of supercapacitors is that they have unsatisfactory energy density.[5] Nowadays, consequently, many research efforts have been focused on improving the energy density of supercapacitors without sacrificing their power density and cycle life.[6−9]

The energy density of supercapacitors can be calculated by the equation of $E = 1/2CV^2$, where E is the energy density, C is the specific capacitance, and V is the cell voltage. Accordingly, the energy density of the supercapacitors can be enhanced by increasing the specific capacitance with development of novel electrode materials and/or broadening the cell voltage which can be efficiently achieved by using organic electrolytes or constructing asymmetric supercapacitors.[10] However, organic electrolytes usually suffer from high cost, poor ionic conductivity, flammability, and high toxicity, which limit their further practical applications.[8,11,12] A promising alternative is to use more environmentally benign aqueous electrolytes that have higher ionic conductivity for supercapacitors.[13] On the other hand, the relatively low voltage of aqueous electrolytes can be partially

Received: June 3, 2013
Accepted: August 2, 2013
Published: August 2, 2013

compensated by use of the pseudocapacitive materials with a high specific capacitance.[14] Hence, the development of novel electrode materials with high specific capacitance and assembly of asymmetric supercapacitors to overcome the issue of low cell voltage, especially in the aqueous systems, can accordingly result in a significantly enhanced energy density.

From the material point of view, various materials such as transition metal oxides, metal hydroxides, conducting polymers, and carbon materials have been extensively investigated as electrode materials in asymmetric supercapacitors. For the anode, activated carbon (AC) is the most widely applied electrode material due to its low cost, high specific surface area, and pore diameter adaptable to the size of ions.[15] With regard to the cathode, various transition metal oxides/metal hydroxides, such as NiO, Co_3O_4, MnO_2, $Ni(OH)_2$, $Co(OH)_2$, etc., have been widely investigated. Among these materials, NiO is considered as a promising candidate due to its low cost, easy availability, and high theoretical specific capacitance.[16,17] However, compared to AC commonly used as anode in commercial supercapacitors, NiO still presents some obvious drawbacks (e.g., low conductivity, poor stability, etc.). In particular, pure NiO has a cubic structure and is classified as a Mott-Hubbard insulator with room temperature conductivity less than 10^{-13} S cm^{-1}, which will greatly reduce its electrochemical properties.[18−20] Recently, some reports indicated that the conductivity of $NiCo_2O_4$ obtained by incorporation of Co into NiO could be greatly enhanced, which is at least 2 orders of magnitude higher than that of monometallic NiO,[21,22] and thus, various $NiCo_2O_4$ nanostructures with high electrochemical performances have been successfully synthesized.[23−26] The enhanced electrochemical properties were mainly attributed to the higher electron conductivity of $NiCo_2O_4$ in comparison with pure NiO or Co_3O_4.[27] On the basis of this, many binary transition metal oxides, such as $NiMn_2O_4$,[28] α-$NiMoO_4$,[29] $CoMoO_4{\cdot}0.9H_2O$ nanorods,[30] $MnMoO_4$−$CoMoO_4$ nanowires,[31] and $CoMoO_4$−$NiMoO_4{\cdot}xH_2O$ bundles[32] have been successfully synthesized and employed as electrode materials for supercapacitors with high capacitance. At present, the design and synthesis of novel binary transition metal oxides with high electron conductivity and good electrochemical performances are still a research hot spot.

As reported in some literatures, the binary metal oxide of nickel tungstate ($NiWO_4$) presents a conductivity on the order of 10^{-7}−10^{-3} S cm^{-1} at different temperatures.[33,34] Obviously, the incorporation of W atoms can greatly enhance the conductivity of $NiWO_4$ in comparison with pure NiO. Thusly, $NiWO_4$ is predicted to represent high electrochemical performance. It has been demonstrated that $NiWO_4$ has excellent catalytic properties.[35,36] However, no literature is found on the application of $NiWO_4$ nanostructure as electrode material for supercapacitors until now. Therefore, in the present work, the amorphous $NiWO_4$ nanostructure was synthesized through a simple coprecipitation process and applied as electrode material for supercapacitors. By assembling NiW-70//AC asymmetric supercapacitor, the obtained device can be operated reversibly between 0 and 1.6 V and displays a high specific capacitance of 71.1 F g^{-1} at 0.25 A g^{-1}, which can deliver a maximum energy density of 25.3 Wh kg^{-1} at a power density of 200 W kg^{-1}. Furthermore, it also presents long cycle life along with 91.4% specific capacitance being retained after 5000 consecutive cycles.

2. EXPERIMENTAL SECTION

2.1. Synthesis of $NiWO_4$ Nanostructure. All reagents were of analytical grade and directly used without any purification. $NiWO_4$ nanostructure was prepared via a simple coprecipitation method by mixing $Na_2WO_4{\cdot}2H_2O$ and $NiCl_2{\cdot}6H_2O$ in a flask under mild stirring. In a typical synthesis, 4.0 mmol of $NiCl_2{\cdot}6H_2O$ was dissolved in 50 mL of distilled water and stirred at 70 °C for about 10 min. Then, 20 mL of distilled water containing 4.0 mmol of $Na_2WO_4{\cdot}2H_2O$ was added dropwise. The adding process was maintained for 30 min, and the resulting suspension was further stirred at 70 °C for 3 h. Finally, the precipitate was separated by centrifugation, rinsed with large amounts of water to remove the remaining reagents, and vacuum-dried at 60 °C for further characterization. Similarly, a series of $NiWO_4$ samples was also prepared at different reaction temperatures (25, 40, 55, and 85) and denoted as NiW-*x*, where *x* represents the reaction temperatures. Furthermore, in order to increase the crystallinity of the as-prepared samples, the obtained NiW-70 was subsequently calcined at 600 °C for 1 h and denoted as NiW-600.

2.2. Material Characterizations. The morphology and microstructure of the samples were characterized by field-emission scanning electron microscopy (FESEM, JSM-6701F, JEOL, Japan), transmission electron microscopy (TEM, JEM-2010, JEOL, Japan), Raman spectroscopy (Renishaw, In Via, UK, with 633 nm line of Ar ion laser as an excitation source), N_2 adsorption−desorption isotherms (Micromeritics ASAP 2020 analyzer, USA), X-ray diffraction patterns (XRD, Rigaku D/MAX 2400 diffractometer, Japan) using Cu Kα radiation, λ = 1.5406 Å, operating at 40 kV and 60 mAy, and X-ray photoelectron spectrometry (XPS, ESCALAB 210, VG Scientific, UK) using Mg Kα radiation under a pressure of 5×10^{-9} Torr.

2.3. Electrochemical Measurements. Commercial AC (Fujian Xinsen Carbon Co. Ltd., China, with a specific surface area of 2000 m^2 g^{-1}) was used as received without further treatment. The working electrodes were prepared by pressing mixtures of the electroactive material, acetylene black, conducting graphite, and polytetrafluoroethylene (PTFE) binder (weight ratio of 80:7.5:7.5:5) onto a nickel foam current collector. The electrochemical measurement of the individual electrode was performed in a three-electrode system, in which Pt foil and Ag/AgCl electrodes were used as counter and reference electrodes, respectively. Each working electrode contained about 4.0 mg of electroactive material and had a geometric surface area of about 1 cm^2. The asymmetric supercapacitor was assembled by separating the NiW-70 and AC electrodes with a separator (Figure 1) and performed in a two-electrode system without the removal of oxygen from the solution. The loading mass ratio of active materials (NiW-70/AC) was estimated to be 0.70 based on the cell voltage, and the specific capacitances were calculated from galvanostatic discharging curves in a three-electrode system. Therefore, the weights of cathode and anode were calculated to be 4.0 and 5.7 mg, respectively. Cyclic voltammetry (CV), galvanostatic charge−discharge, and electrochemical impedance spectroscopy (EIS) measurements were carried out in these three-electrode and two-electrode systems. EIS measurement was tested at the frequency range of 100 kHz to 10 mHz with an AC amplitude of 5 mV under an open

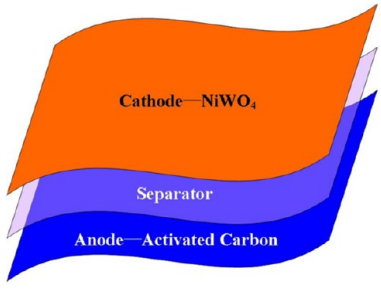

Figure 1. Schematic illustration of the assembled asymmetric supercapacitor by using $NiWO_4$ as cathode and AC as anode in aqueous KOH electrolyte.

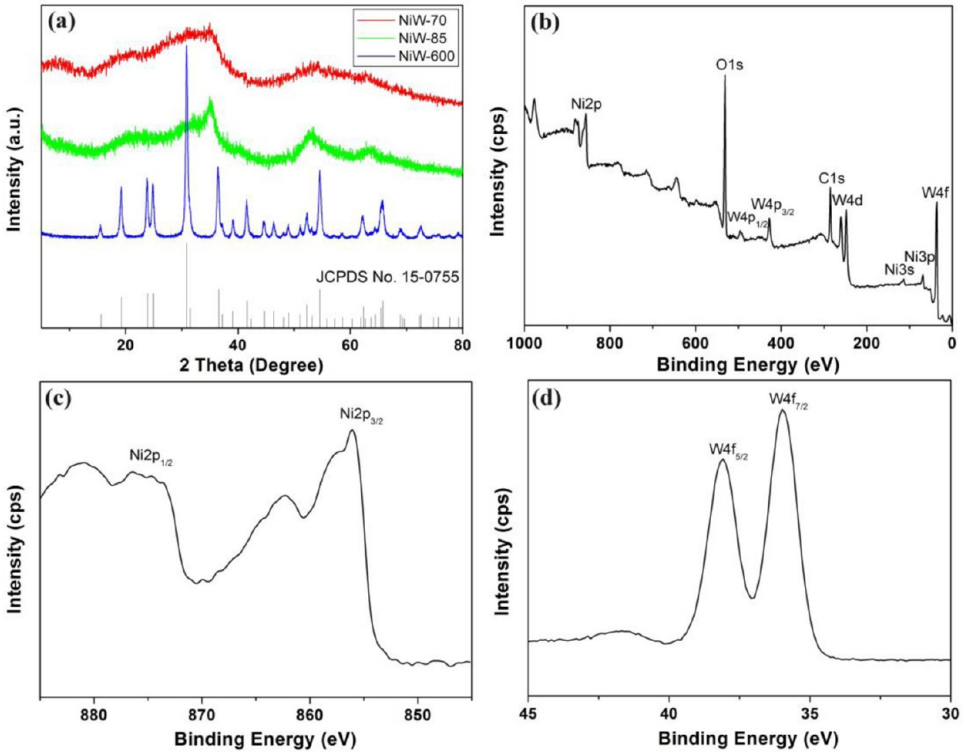

Figure 2. XRD patterns of NiW-*x* (a), XPS survey spectrum (b), Ni2p spectrum (c), and W4f spectrum (d) of NiW-70 nanostructure.

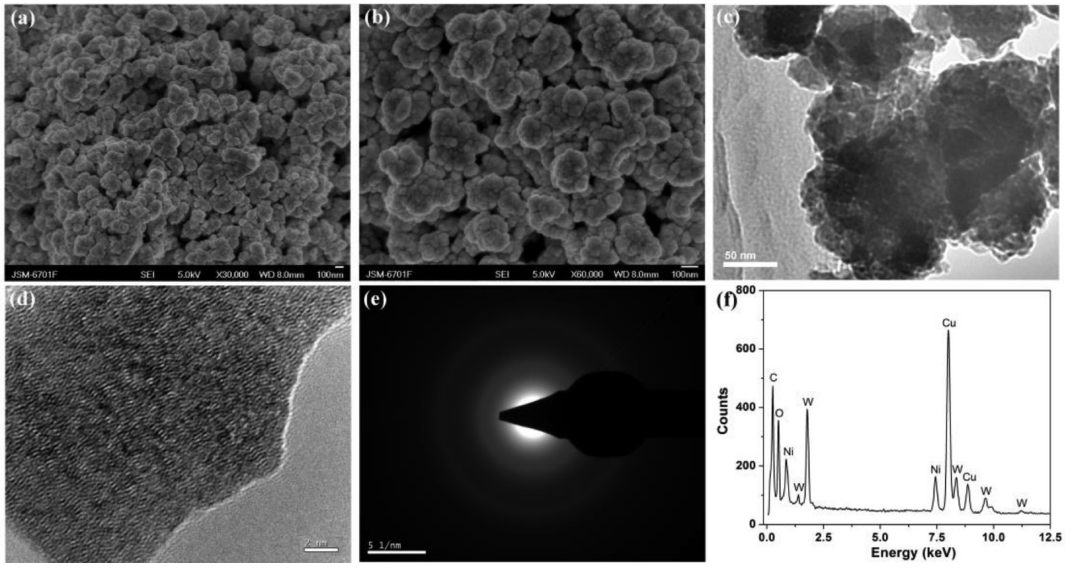

Figure 3. Low-magnification (a) and high-magnification (b) FESEM images, TEM image (c), HRTEM image (d), SAED pattern (e), and the corresponding EDS curve (f) of NiW-70 nanostructure.

circuit potential of 0.3 V. All of the above electrochemical measurements were carried out on a CHI 660C (Shanghai, China) electrochemical workstation at room temperature by using 2 M KOH solution as the aqueous electrolyte. The cyclic stability of the electrode was also evaluated by a Land Battery Test System (Wuhan Kingnuo Electronic Company, CT2001A, China).

3. RESULTS AND DISCUSSION

3.1. Characterizations of $NiWO_4$ Nanostructure. In this study, $NiWO_4$ was prepared by a coprecipitation method through the reaction of $NiCl_2{\cdot}6H_2O$ and $Na_2WO_4{\cdot}2H_2O$ in a molar ratio of 1:1. Addition of WO_4^{2-} ions into the $NiCl_2$ solution would cause the production of $NiWO_4$ precipitate according to the following reaction 1:[37−39]

$$Ni^{2+}\,(aq) + WO_4^{2-}\,(aq) \rightarrow NiWO_4\,(s) \qquad (1)$$

Noticeably, the as-prepared samples were washed with large amounts of water to remove the byproduct of sodium chloride, and the precipitate should be the pure $NiWO_4$.

Figure 2a shows the XRD patterns of the as-prepared samples. Evidently, the powders of NiW-70 and NiW-85 were amorphous without any crystallized phases. Namely, the broad nature and low intensity of the diffraction peaks should result from the

dx.doi.org/10.1021/am402127u | ACS Appl. Mater. Interfaces 2013, 5, 8044−8052

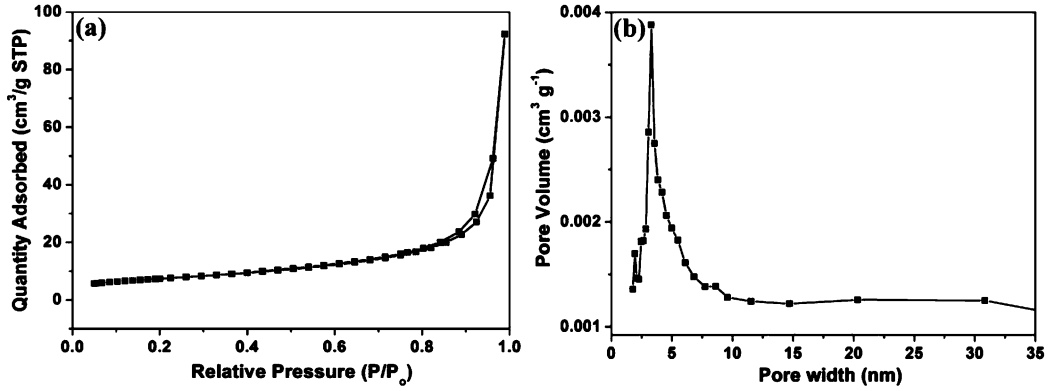

Figure 4. N_2 adsorption−desorption isotherm (a) and BJH adsorption pore size distribution of NiW-70 nanostructure (b).

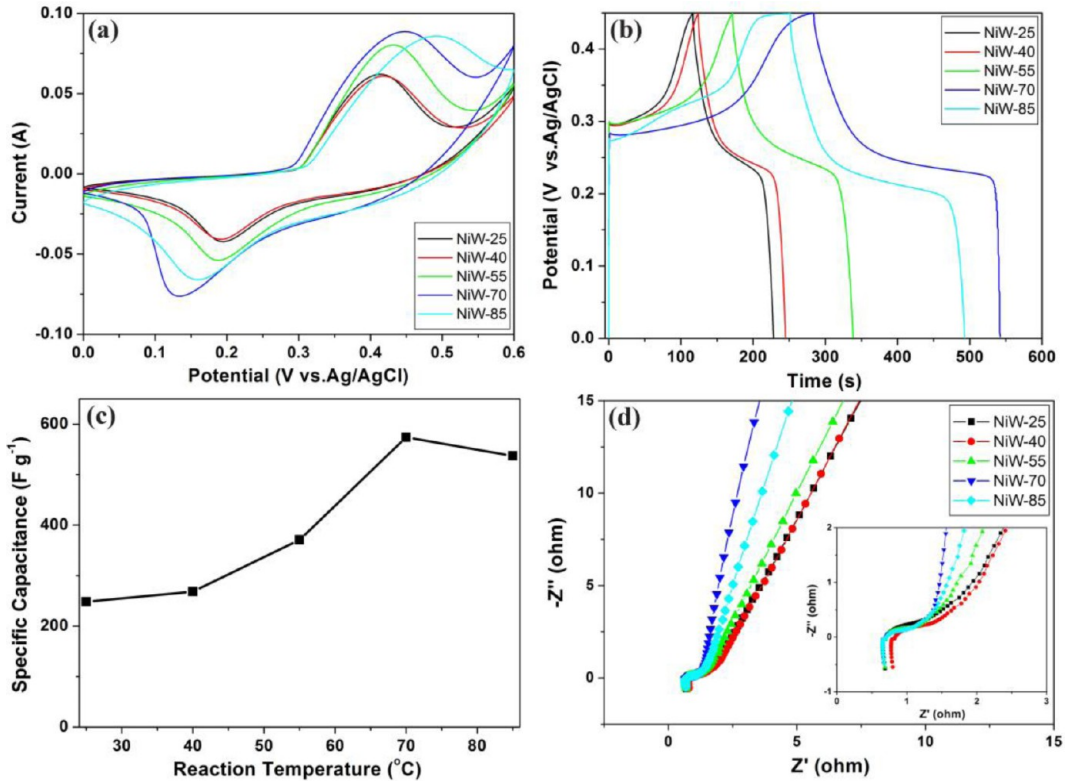

Figure 5. CV curves at 20 mV s^{-1} (a), galvanostatic charge−discharge curves at 1 A g^{-1} (b), the specific capacitance calculated from discharge curves at 1 A g^{-1} (c), and EIS plots (d) of NiW-*x* electrode synthesized at different temperatures in 2 M KOH aqueous electrolyte.

amorphous state and/or nanometer-scale size of the as-prepared $NiWO_4$. To increase the crystallinity of the as-prepared samples, the NiW-70 was calcined at 600 °C for 1 h, and the corresponding NiW-600 can be perfectly indexed to the standard crystal $NiWO_4$ structure from its XRD pattern[40] (JCPDS card No. 15-0755) and Raman spectrum[41] (Figure S1, Supporting Information). For further understanding of the chemical composition of the prepared NiW-70 sample, XPS analysis was also performed. In the survey spectrum of the sample (Figure 2b), many distinct Ni signals (2s, 2p, 3s, 3p) and W signals (4s, 4p, 4d, 4f) appeared in addition to the O1s signal. From the high-resolution Ni 2p spectrum shown in Figure 2c, the Ni $2p_{3/2}$ peak at 856.1 eV implies the presence of Ni ions in the form of divalent state.[42] Moreover, the W $4f_{7/2}$ peak appearing at 36.0 eV (Figure 2d) and combining with the Ni $2p_{3/2}$ peak at 856.1 eV together suggests the formation of $NiWO_4$ binary metal oxide.[43] In addition, element analysis by XPS reveals that the atomic ratio of Ni to W is close to 1:1, confirming the successful synthesis of $NiWO_4$.

The morphology and structure characters of the NiW-70 are shown in Figure 3. It can be clearly observed from FESEM images that the NiW-70 is composed of cauliflower-like architecture, and each flower is randomly assembled by dozens of tiny individual nanoparticles with some extent of agglomeration. The FESEM and TEM images jointly indicate that some mesoporous microstructures were formed from the surface to the inside within the NiW-70 structure. Simultaneously, both the HRTEM image and the corresponding selected-area electron diffraction (SAED) pattern of NiW-70 have proven the amorphous characteristic of the NiW-70 nanostructure (Figure 3d,e), which is in good agreement with the previous XRD result presented in Figure 2a. Besides, the energy dispersive X-ray spectroscopy (EDS) analysis also demonstrates the presence of Ni, W, and O elements, which is in good accordance with the

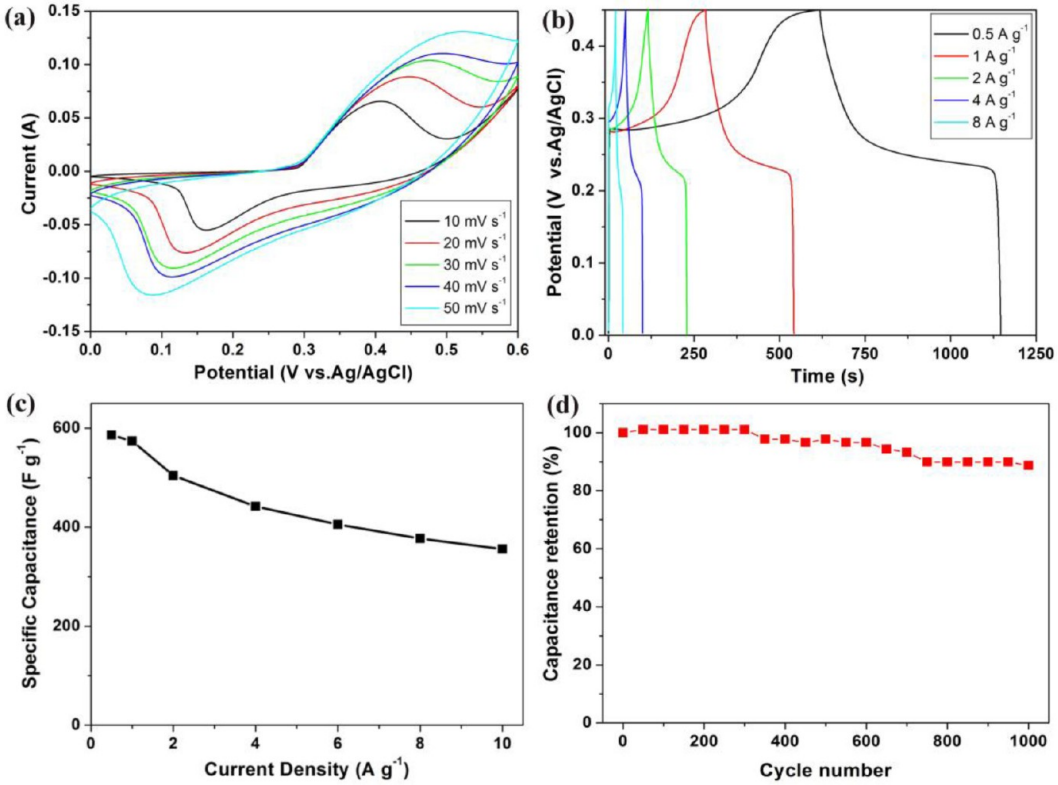

Figure 6. CV curves at different scan rates (a), galvanostatic charge–discharge curves at different current densities (b), the specific capacitance calculated from discharge curves at different current densities (c), and the cycle life (d) of NiW-70 electrode in 2 M KOH aqueous electrolyte.

XPS results (Figure 3d). Further information on the specific surface area and pore structure of the as-prepared NiW-70 was obtained from N_2 adsorption–desorption isotherm measurements. The isotherm profile displays a typical III characteristic with a distinct hysteresis loop observed in the range of 0.75–0.95 p/p_o (Figure 4a). The Brunauer–Emmett–Teller (BET) specific surface area is calculated to be 26.3 $m^2\ g^{-1}$ with a total pore volume of 0.14 $cm^3\ g^{-1}$. Barrett–Joyner–Halenda (BJH) analysis indicates that the pores have a mainly mesoporous structure with a pore size distribution of 2–10 nm centered at about 3.3 nm (Figure 4b). Such a pore size distribution is favorable to improve the electrochemical behavior of the NiW-70 electrode due to the unhindered diffusion and accession of electrolyte ions into the inner space/matrix.[4,44]

3.2. Electrochemical Characterizations of the Nanostructured $NiWO_4$ Electrode. As indicated by BET results, the amorphous $NiWO_4$ with porous structure may have potential applications in supercapacitors. CV, galvanostatic charge–discharge, and EIS tests were performed to evaluate the electrochemical capacitive properties of the as-prepared NiW-*x* in 2 M KOH aqueous electrolyte. Figure 5a displays the typical CV curves of the various NiW-*x* electrodes at 20 mV s^{-1}. All the CV curves consist of a pair of strong redox peaks, suggesting that the measured capacitance is mainly governed by the Faradaic redox mechanism, and the reaction is based on the reversible redox of Ni^{2+} to Ni^{3+}:[29]

$$Ni^{2+} \underset{\text{discharge}}{\overset{\text{charge}}{\rightleftharpoons}} Ni^{3+} + e^- \qquad (2)$$

From the Pourbaix diagram of W element shown in Figure S2, Supporting Information, the W does not involve any redox reaction; thereby, the redox behavior of W has no contribution to the measured capacitance. This is in good accordance with the previous reports about $MnMoO_4/CoMoO_4$ as electrode materials for supercapacitors, where the pseudocapacitance comes from the faradic redox reaction of both Mn and Co, and Mo does not participate in any redox reaction.[31] Actually, the main function of W element in this system is to improve the conductivity of $NiWO_4$ material and then to achieve the enhaced electrochemical capacitance.

Among all the samples, the NiW-70 electrode displays a larger CV curve area than other counterparts, suggesting it has the highest energy storage capacity. To evaluate the capacitance of the NiW-*x* electrode materials, a galvanostatic charge–discharge test was performed at a current density of 1 A g^{-1} (Figure 5b). The specific capacitance can be calculated according to the eq 3:

$$C_m = C/m = I \times \Delta t/(\Delta V \times m) \qquad (3)$$

where C_m (F g^{-1}) is the specific capacitance, I (mA) is the charge–discharge current, Δt (s) is the discharging time, ΔV (V) represents the potential drop during discharge, and m (mg) is the mass of the active material within the electrode. Obviously, NiW-70 electrode possesses the maximum charging and discharging times, resulting in the highest specific capacitance. The corresponding specific capacitances calculated from discharging times for NiW-25 to NiW-85 are 248.2, 268.4, 370.7, 574, and 536.9 F g^{-1}, respectively (Figure 5c). It is notable that the electrochemical property of NiW-600 is much less than NiW-70 electrode. Considering that the electrochemical performance of $NiWO_4$ material largely depends on its surface microstructure, we believed that both the composition change (structural water removal and residual organic matter decomposition)[22,45–47] and the surface area reduction[48,49] contributed to the significant loss in the specific capacitance of high crystalline NiW-600, and thus,

dx.doi.org/10.1021/am402127u | ACS Appl. Mater. Interfaces 2013, 5, 8044–8052

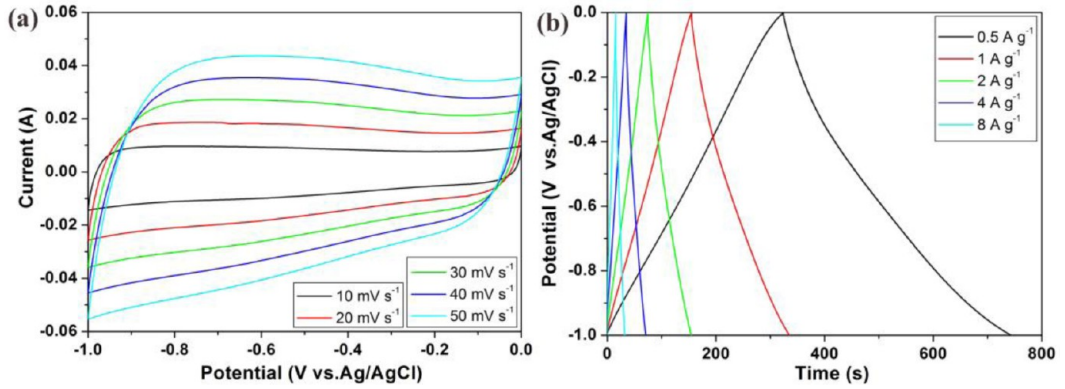

Figure 7. CV curves at different scan rates (a) and galvanostatic charge−discharge curves at different current densities (b) of AC electrodes performed in a three-electrode system in the 2 M KOH electrolyte.

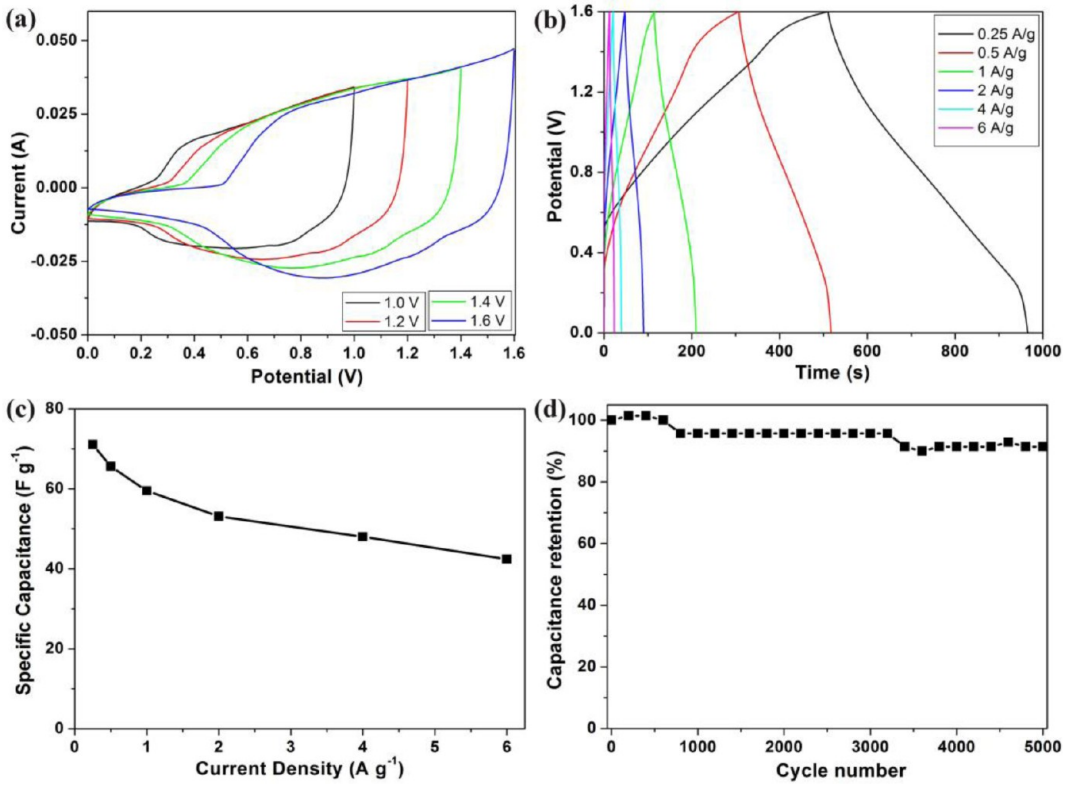

Figure 8. CV curves measured at 40 mV s^{-1} with different potential windows (a), galvanostatic charge−discharge curves measured at different current densities between 0 and 1.6 V (b), the specific capacitance calculated from discharge curves at different current density (c), and the cycle life (d) of NiW-70//AC asymmetric supercapacitor in 2 M KOH aqueous electrolyte.

amorphous NiW-70 is more suitable to be applied as electrode material for supercapacitors. Moreover, the same results were also observed for amorphous MnO_2 and $Ni(OH)_2$ which have higher capacitance than their crystalline counterparts.[50,51]

EIS measurements were also carried out to evaluate the charge transfer and electrolyte diffusion in the electrode/electrolyte interface, as shown in Figure 5d. Obviously, the EIS of the NiW-*x* electrode was composed of a semicircle at the high-frequency region and a straight line at the low-frequency region. At the high-frequency region, the internal resistance and charge transfer resistance of the five samples are almost the same. However, the NiW-70 electrode exhibits lower diffusive resistance (Warburg impedance) than other samples at the low-frequency region according to the high slope of the straight line. Since Warburg resistance is related to the ion diffusion/transport in the electrolyte, the lower Warburg resistance will facilitate the diffusion of electrolyte ions (OH^-) into the electrode materials;[52] accordingly, a facile and reversible Faradaic redox would be taken,[53] and a good electrochemical property could be realized for the NiW-70 electrode.

To further verify the pseudocapacitance contribution, typical CV curves of the NiW-70 electrode at a variety of scan rates varying from 10 to 50 mV s^{-1} are shown in Figure 6a. With an increase in the scan rates, the current subsequently increases while the CV shape changes little, and rapid current response on voltage reversal occurs at each end potential, revealing its good electrochemical capacitance.[54] Furthermore, the symmetric characteristic of the anodic and cathodic peaks indicates the excellent reversibility of the electrode. On the other hand, the rate capability of the as-synthesized material is a significant

dx.doi.org/10.1021/am402127u | ACS Appl. Mater. Interfaces 2013, 5, 8044−8052

consideration required for practical applications in supercapacitors. Figure 6b provides the galvanostatic charge−discharge curves at different current densities. The specific capacitances of NiW-70 electrode calculated from discharging time according to eq 3 are 586.2, 574.0, 504.4, 441.8, and 376.9 F g^{-1}, corresponding to the current densities of 0.5, 1, 2, 4, and 8 A g^{-1}, respectively (Figure 6c). Apparently, 64% of capacitance is still retained when the current density increases from 0.5 to 8 A g^{-1}, suggesting that the NiW-70 electrode possesses outstanding high-rate capability. The high electrochemical performance can be attributed to the enhanced conductivity and porous microstructure of amorphous NiW-70 which facilitates the penetration of electrolytes into the inner part and shortens the ionic diffusion path.[55] The stability of the nanostructured NiW-70 over 1000 times of continuous cycling at 2 A g^{-1} is shown in Figure 6d. It is clearly obtained that the capacitance decreases gradually with cycling, and an approximately 10% loss of capacitance is observed after 1000 cycles. All of the above characterizations suggest that the NiW-70 has high electrochemical performance, and it is suitable as cathode material for asymmetric supercapacitors.

3.3. Electrochemical Characterizations of the NiW-70//AC Asymmetric Supercapacitor. To obtain a high energy density, an asymmetric supercapacitor was assembled by use of NiW-70 and AC as cathode and anode electrodes, respectively (Figure 1). As for an asymmetric supercapacitor, it is necessary to balance the charges stored at the cathode and anode, namely, $q_+ = q_-$.[8,56] The stored charge is related to the specific capacitance (C_m), the potential window for the charge−discharge process (ΔV), and the mass of the electrode (m), which is following the eq 4:

$$q = C_m \times (\Delta V) \times m \quad (4)$$

From the charge−discharge test, the NiW-70 electrode presents a specific capacitance of 574 F g^{-1} at a discharge current of 1 A g^{-1}, while the AC electrode owns a specific capacitance of 180.8 F g^{-1} (Figure 7b). Therefore, on the basis of the specific capacitances and the potential windows of the two materials, the optimum loading mass ratio of NiW-70/AC was estimated to be 0.70 in the asymmetric supercapacitor.

Figure 8a gives CV curves of the NiW-70//AC asymmetric supercapacitor at different potential windows in 2 M KOH aqueous solution at 40 mV s^{-1}. The weights of cathode and anode are 4.0 and 5.7 mg, respectively, and each electrode has a geometric surface area of about 1 cm^2. The assembled asymmetric supercapacitor shows a broad redox peak and can be cycled between 0 and 1.6 V with a good reversibility. Accordingly, the potential window of 0−1.6 V was chosen for the following investigation of the overall electrochemical performances of the asymmetric supercapacitor. Figure 8b shows the galvanostatic charge−discharge curves of the NiW-70//AC asymmetric supercapacitor measured at different current densities of 0.25, 0.5, 1, 2, 4, and 6 A g^{-1} in the 2 M KOH aqueous electrolyte, which presents nearly a linear variation within 0−1.6 V. The specific capacitances calculated from the galvanostatic charge−discharge curves according to eq 3 are 71.1, 65.6, 59.5, 53.1, 48.0, and 42.4 F g^{-1} at current densities of 0.25, 0.5, 1, 2, 4, and 6 A g^{-1}, respectively (Figure 8c). Furthermore, it can be observed that all the discharge curves are nearly symmetric with their corresponding charging counterparts, demonstrating the excellent electrochemical reversibility and good Coulombic efficiency. The cycling stability of the asymmetric supercapacitor was further investigated by galvanostatic charge−discharge between 0 and 1.6 V at a current density of 1.0 A g^{-1} (Figure 8d). Results have shown that the hybrid supercapacitor retains 91.4% of initial capacitance even after 5000 consecutive cycles of charge−discharge testing, displaying an excellent cycling ability of NiW-70//AC asymmetric supercapacitor. This retention is better than the previous reported samples of $Ni(OH)_2$/CNT/NF//AC (83% after 3000 cycles),[57] $NiCo_2O_4$−rGO//AC (83% after 2500 cycles),[27] Ni−Co oxide//AC (85% after 2000 cycles),[16] $Ni(OH)_2$/graphene//CMK-5 (90% after 5000 cycles),[58] and comparable to those of $Ni(OH)_2$/graphene//porous graphene (94.3% after 3000 cycles)[59] and Ni_xCo_{1-x} LDH−ZTO//AC (92.7% after 5000 cycles)[60] asymmetric supercapacitors.

Figure 9 provides the Ragone plots related to the corresponding energy and power density. The energy density

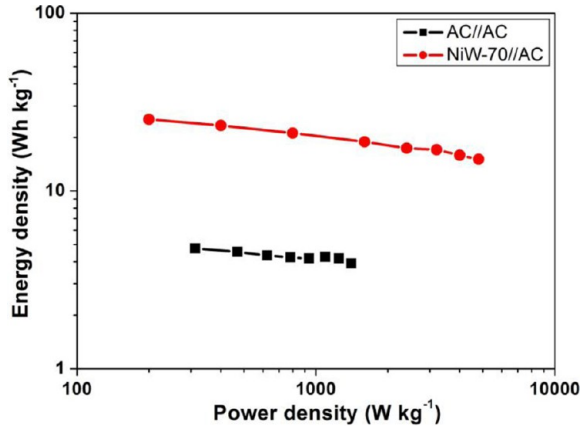

Figure 9. Ragone plots of the as-assembled NiW-70//AC asymmetric supercapacitor.

(E) at a power density (P) was calculated according to eqs 5 and 6:

$$E = 1/2 \times C_m \times (\Delta V)^2 \quad (5)$$

$$P = E/\Delta t \quad (6)$$

It can be clearly seen that the NiW-70//AC asymmetric supercapacitor exhibits much higher energy density than the AC//AC symmetric supercapacitor. The NiW-70//AC asymmetric supercapacitor can deliver a high energy density of 25.3 Wh kg^{-1} at a power density of 200 W kg^{-1} and still retain 15.1 Wh kg^{-1} at a high power density of 4.8 KW kg^{-1}. The high energy density of NiW-70//AC asymmetric supercapacitor can be attributed to both the high specific capacitance and the large cell voltage in the aqueous electrolyte. Furthermore, the NiW-70//AC asymmetric supercapacitor presents an improved energy density at high power density compared to previously reported Ni−Co oxide//AC (7.4 Wh kg^{-1} at 1.9 KW kg^{-1}),[16] Ni_xCo_{1-x} LDH−ZTO//AC (9.7 Wh kg^{-1} at 5.82 KW kg^{-1}),[60] $NaMnO_2$//AC (13.2 Wh kg^{-1} at 1.0 KW kg^{-1}),[61] MnO_2 nanorods//AC (17 Wh kg^{-1} at 2.0 KW kg^{-1}),[62] $LiTi_2(PO_4)_3$//AC (15 Wh kg^{-1} at 1.0 KW kg^{-1}),[63] and $MnFe_2O_4$@C/$LiMn_2O_4$ (5.5 Wh kg^{-1} at 1.8 KW kg^{-1})[64] asymmetric configurations. Thusly, all of these attractive results demonstrated that the low cost NiW-70//AC asymmetric supercapacitor systems under environmentally friendly aqueous electrolytes with high energy density would be a very promising energy storage system in electric vehicles and hybrid electric vehicles.

4. CONCLUSIONS

In summary, a series of amorphous $NiWO_4$ nanostructure was successfully synthesized by a simple coprecipitation method. The nanostructured NiW-70 was applied as electrode material for supercapacitors and exhibited a high specific capacitance of 586.2 F g^{-1} at 0.5 A g^{-1} in a three-electrode system. An asymmetric supercapacitor device is successfully assembled by use of NiW-70 and AC as the cathode and anode, respectively, which can be cycled reversibly in the high-voltage region of 0−1.6 V, delivers a high energy density of 25.3 Wh kg^{-1} at a power density of 200 W kg^{-1}, and can still operate at a high power density of 4.8 kW kg^{-1} with an energy density of 15.1 Wh kg^{-1}. Furthermore, this supercapacitor also exhibits an excellent long cycle life along with 91.4% specific capacitance being retained after 5000 consecutive cycles. These properties make NiW-70//AC a promising candidate for future energy storage applied in hybrid electric vehicles and electric vehicles.

■ ASSOCIATED CONTENT

Ⓢ Supporting Information

Raman spectrum of NiW-600 and Pourbaix diagram of W element. This material is available free of charge via the Internet at http://pubs.acs.org.

■ AUTHOR INFORMATION

Corresponding Author

*E-mail: jqwang@licp.cas.cn. Fax: +86-931-8277088. Tel.: +86-931-4968076.

Notes

The authors declare no competing financial interest.

■ ACKNOWLEDGMENTS

We are thankful for the financial support from the National Natural Science Foundation of China (Grant Nos. 51075384 and 51205385) and the "Funds for Distinguished Young Scientists of Gansu Province".

■ REFERENCES

(1) Chien, H. C.; Cheng, W. Y.; Wang, Y. H.; Lu, S. Y. *Adv. Funct. Mater.* **2012**, *22*, 5038−5043.
(2) Conway, B. E. In *Electrochemical Supercapacitors: Scientific Fundamentals and Technological Applications*; Conway, B. E., Ed.; Kluwer Academic/Plenum Publishers: New York, 1999.
(3) Miller, J. R.; Simon, P. *Science* **2008**, *321*, 651−652.
(4) Simon, P.; Gogotsi, Y. *Nat. Mater.* **2008**, *7*, 845−854.
(5) Salunkhe, R. R.; Jang, K.; Lee, S.; Yu, S.; Ahn, H. *J. Mater. Chem.* **2012**, *22*, 21630−21635.
(6) Burke, A. *J. Power Sources* **2000**, *91*, 37−50.
(7) Izadi-Najafabadi, A.; Yasuda, S.; Kobashi, K.; Yamada, T.; Futaba, D. N.; Hatori, H.; Yumura, M.; Iijima, S.; Hata, K. *Adv. Mater.* **2010**, *22*, E235−E241.
(8) Chen, P.; Shen, G. Z.; Shi, Y.; Chen, H. T.; Zhou, C. W. *ACS Nano* **2010**, *4*, 4403−4411.
(9) Jiang, H.; Lee, P. S.; Li, C. Z. *Energy Environ. Sci.* **2013**, *6*, 41−53.
(10) Zhang, J. T.; Jiang, J. W.; Li, H. L.; Zhao, X. S. *Energy Environ. Sci.* **2011**, *4*, 4009−4015.
(11) Fan, Z. J.; Yan, J.; Wei, T.; Zhi, L. J.; Ning, G. Q.; Li, T. Y.; Wei, F. *Adv. Funct. Mater.* **2011**, *21*, 2366−2375.
(12) Jiang, H.; Li, C. Z.; Sun, T.; Ma, J. *Nanoscale* **2012**, *4*, 807−812.
(13) Lu, X. H.; Yu, M. H.; Wang, G. M.; Zhai, T.; Xie, S. L.; Ling, Y. C.; Tong, Y. X.; Li, Y. *Adv. Mater.* **2013**, *25*, 267−272.
(14) Xu, C. J.; Du, H. D.; Li, B. H.; Kang, F. Y.; Zeng, Y. Q. *J. Electrochem. Soc.* **2009**, *156*, A435−A441.
(15) Demarconnay, L.; Raymundo-Piñero, E.; Béguin, F. *J. Power Sources* **2011**, *196*, 580−586.
(16) Tang, C. H.; Tang, Z.; Gong, H. *J. Electrochem. Soc.* **2012**, *159*, A651−A656.
(17) Fan, L.; Tang, L.; Gong, H. F.; Yao, Z. H.; Guo, R. *J. Mater. Chem.* **2012**, *22*, 16376−16381.
(18) Morin, F. J. *Phys. Rev.* **1954**, *93*, 1199−1204.
(19) Biju, V.; Khadar, M. A. *Mater. Res. Bull.* **2001**, *36*, 21−33.
(20) Bhatt, A. S.; Bhat, D. K.; Santosha, M. S.; Tai, C. *J. Mater. Chem.* **2011**, *21*, 13490−13497.
(21) Tarasevich, M. R.; Efremov, B. N. In *Electrodes of Conductive Metallic Oxides Part A*; Trasatti, S., Ed.; Elsevier: Amsterdam, 1980.
(22) Wei, T. Y.; Chen, C. H.; Chien, H. C.; Lu, S. Y.; Hu, C. C. *Adv. Mater.* **2010**, *22*, 347−351.
(23) Wang, X.; Han, X. D.; Lim, M. F.; Singh, N.; Gan, C. L.; Ma, J.; Lee, P. S. *J. Phys. Chem. C* **2012**, *116*, 12448−12454.
(24) Jiang, H.; Ma, J.; Li, C. Z. *Chem. Commun.* **2012**, *48*, 4465−4467.
(25) Chang, J.; Sun, J.; Xu, C. H.; Xu, H.; Gao, L. *Nanoscale* **2012**, *4*, 6786−6791.
(26) Wang, C. H.; Zhang, X.; Zhang, D. C.; Yao, C.; Ma, Y. W. *Electrochim. Acta* **2012**, *63*, 220−227.
(27) Wang, X.; Liu, W. S.; Lu, X. H.; Lee, P. S. *J. Mater. Chem.* **2012**, *22*, 23114−23119.
(28) Zhang, M.; Guo, S. H.; Zheng, L.; Zhang, G. N.; Hao, Z. P.; Kang, L. P.; Liu, Z. H. *Electrochim. Acta* **2013**, *87*, 546−553.
(29) Senthilkumar, B.; Sankar, K. V.; Selvan, R. K.; Danielle, M.; Manickam, M. *RSC Adv.* **2013**, *3*, 352−357.
(30) Liu, M. C.; Kong, L. B.; Ma, X. J.; Lu, C.; Li, X. M.; Luo, Y. C.; Kang, L. *New J. Chem.* **2012**, *36*, 1713−1716.
(31) Mai, L. Q.; Yang, F.; Zhao, Y. L.; Xu, X.; Xu, L.; Luo, Y. Z. *Nat. Commun.* **2011**, *2*, 381.
(32) Liu, M. C.; Kong, L. B.; Lu, C.; Ma, X. J.; Li, X. M.; Luo, Y. C.; Kang, L. *J. Mater. Chem. A* **2013**, *1*, 1380−1387.
(33) Bharati, R.; Singh, R. A. *J. Mater. Sci.* **1980**, *15*, 1293−1296.
(34) Bharati, R.; Singh, R. A. *J. Mater. Sci.* **1983**, *18*, 1540−1542.
(35) Bi, Y. F.; Nie, H.; Li, D. D.; Zeng, S. Q.; Yang, Q. H.; Li, M. F. *Chem. Commun.* **2010**, *46*, 7430−7432.
(36) García-Pérez, U. M.; Martínez-de la Cruz, A.; Peral, J. *Electrochim. Acta* **2012**, *81*, 227−232.
(37) Parhi, P.; Karthik, T. N.; Manivannan, V. *J. Alloys Compd.* **2008**, *465*, 380−386.
(38) Montini, T.; Gombac, V.; Hameed, A.; Felisari, L.; Adami, G.; Fornasiero, P. *Chem. Phys. Lett.* **2010**, *498*, 113−119.
(39) Farsi, H.; Hosseini, S. A. *J. Solid State Electrochem.* **2013**, *17*, 2079−2086.
(40) He, H. Y. *Mater. Res. Innovations* **2008**, *12*, 138−141.
(41) Ross-Medgaarden, E. I.; Wachs, I. E. *J. Phys. Chem. C* **2007**, *111*, 15089−15099.
(42) Shin, W. H.; Jeong, H. M.; Kim, B. G.; Kang, J. K.; Choi, J. W. *Nano Lett.* **2012**, *12*, 2283−2288.
(43) Mancheva, M. N.; Iordanova, R. S.; Klissurski, D. G.; Tyuliev, G. T.; Kunev, B. N. *J. Phys. Chem. C* **2007**, *111*, 1101−1104.
(44) Meher, S. K.; Justin, P.; Rao, G. R. *ACS Appl. Mater. Interfaces* **2011**, *3*, 2063−2073.
(45) Sugimoto, W.; Iwata, H.; Yokoshima, K.; Murakami, Y.; Takasu, Y. *J. Phys. Chem. B* **2005**, *109*, 7330−7338.
(46) Chang, J.; Chen, Y.; Tsai, W. *J. Power Sources* **2004**, *135*, 344−353.
(47) Fang, W.; Huang, J.; Chen, L.; Su, Y. O.; Chen, K. *J. Power Sources* **2006**, *160*, 1506−1510.
(48) Ghaemi, M.; Ataherian, F.; Zolfaghari, A.; Jafari, S. M. *Electrochim. Acta* **2008**, *53*, 4607−4614.
(49) Wu, J. B.; Lin, Y.; Xia, X. H.; Xu, J. Y.; Shi, Q. Y. *Electrochim. Acta* **2011**, *56*, 7163−7170.
(50) Devaraj, S.; Munichandraiah, N. *J. Phys. Chem. C* **2008**, *112*, 4406−4417.
(51) Li, H. B.; Yu, M. H.; Wang, F. X.; Liu, P.; Liang, Y.; Xiao, J.; Wang, C. X.; Tong, Y. X.; Yang, G. W. *Nat. Commun.* **2013**, *4*, 1894.
(52) Liu, M.; Kong, L.; Lu, C.; Li, X.; Luo, Y.; Kang, L. *ACS Appl. Mater. Interfaces* **2012**, *4*, 4631−4636.

(53) Meher, S. K.; Rao, G. R. *J. Phys. Chem. C* **2011**, *115*, 15646−15654.
(54) Yuan, C. Z.; Li, J. Y.; Hou, L. R.; Yang, L.; Shen, L. F.; Zhang, X. G. *J. Mater. Chem.* **2012**, *22*, 16084−16090.
(55) Lu, X. H.; Huang, X.; Xie, S. L.; Zhai, T.; Wang, C. S.; Zhang, P.; Yu, M. H.; Li, W.; Liang, C. L.; Tong, Y. X. *J. Mater. Chem.* **2012**, *22*, 13357−13364.
(56) Khomenko, V.; Raymundo-Piñero, E.; Béguin, F. *J. Power Sources* **2006**, *153*, 183−190.
(57) Tang, Z.; Tang, C. H.; Gong, H. *Adv. Funct. Mater.* **2012**, *22*, 1272−1278.
(58) Wang, Y. G.; Zhou, D. D.; Zhao, D.; Hou, M. Y.; Wang, C. X.; Xia, Y. Y. *J. Electrochem. Soc.* **2013**, *160*, A98−A104.
(59) Yan, J.; Fan, Z. J.; Sun, W.; Ning, G. Q.; Wei, T.; Zhang, Q.; Zhang, R. F.; Zhi, L. J.; Wei, F. *Adv. Funct. Mater.* **2012**, *22*, 2632−2641.
(60) Wang, X.; Sumboja, A.; Lin, M. F.; Yan, J.; Lee, P. S. *Nanoscale* **2012**, *4*, 7266−7272.
(61) Qu, Q. T.; Shi, Y.; Tian, S.; Chen, Y. H.; Wu, Y. P.; Holze, R. *J. Power Sources* **2009**, *194*, 1222−1225.
(62) Qu, Q. T.; Zhang, P.; Wang, B.; Chen, Y. H.; Tian, S.; Wu, Y. P.; Holze, R. *J. Phys. Chem. C* **2009**, *113*, 14020−14027.
(63) Luo, J. Y.; Xia, Y. Y. *J. Power Sources* **2009**, *186*, 224−227.
(64) Lin, Y. P.; Wu, N. L. *J. Power Sources* **2011**, *196*, 851−854.